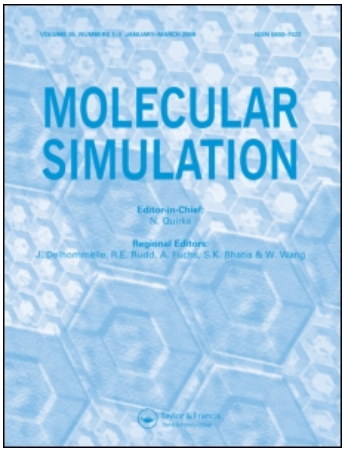

Molecular Simulation
Publication details, including instructions for authors and subscription information:
http://www.informaworld.com/smpp/title~content=t713644482

Mesoscopic dynamics of complex vesicle formation: kinetic versus thermodynamic factors

G. J. A. Sevink[a]; A. V. Zvelindovsky[b]
[a] Leiden Institute of Chemistry, Leiden University, Leiden, RA, The Netherlands [b] Department of Physics, Astronomy and Mathematics, University of Central Lancashire, Preston, United Kingdom

To cite this Article Sevink, G. J. A. and Zvelindovsky, A. V.(2007) 'Mesoscopic dynamics of complex vesicle formation: kinetic versus thermodynamic factors', Molecular Simulation, 33: 4, 405 — 415
To link to this Article: DOI: 10.1080/08927020601133391
URL: http://dx.doi.org/10.1080/08927020601133391

Molecular Simulation, Vol. 33, Nos. 4–5, 15–30 April 2007, 405–415

Taylor & Francis
Taylor & Francis Group

Mesoscopic dynamics of complex vesicle formation: kinetic versus thermodynamic factors

G. J. A. SEVINK†* and A.V. ZVELINDOVSKY‡

†Leiden Institute of Chemistry, Leiden University, PO Box 9502, 2300 RA, Leiden, The Netherlands
‡Department of Physics, Astronomy and Mathematics, University of Central Lancashire, Preston PR1 2HE, United Kingdom

(Received 15 June 2006; in final form 10 November 2006)

We have used dynamic self-consistent field (DSCF) theory to elaborate on our previous study of spontaneous vesicle formation in short amphiphilic systems (G.J.A. Sevink and A.V. Zvelindovsky, *Macromolecules* **2005**, *38*, p. 7502). Here, we focus on the situation where a spherical shape, representing the macrostructure, is imposed from the start. Inside this droplet-like container, the solphophilic and solphophobic blocks are initially mixed. Such experimental starting conditions can be obtained with inktjet techniques, where a droplet of amphiphiles is quenched in solvent. In particular, we consider the interplay between confinement and microstructure for a single droplet. We show that there is a dependency on droplet/cluster size. Large spherical amphiphilic droplets are only favored in case of symmetric amphiphiles, and very asymmetric amphiphiles are rather indifferent of the initial droplet shape. Slightly asymmetric systems prefer larger macrostructures that are non-spherical. We considered mixing of systems with different interfacial properties in detail by induced fusion of droplets of different material, leading to janus-like vesicles. A detailed analysis by means of Minkowski functionals hints once more that most processes in these systems are curvature driven.

Keywords: Micro droplets; Amphiphiles; Spontaneous vesicle; Computer modeling; Dynamic self-consistent field (DSCF)

1. Introduction

Understanding the principles of vesicle evolution is key to the understanding of cellular processes in biology as well as the design and function of self-assembled synthetic vesicles for nanotechnology [1–4]. In biology, lipid membrane fusion and fission are fundamental in processes ranging from fertilization, synapse release, intercellular traffic and viral infection [5,6]. It was recently shown that several block copolymers are also capable of forming vesicles, so-called polymersomes. Since polymersomes have been prepared from a wide range of polymers with intricate properties, they are potentially interesting systems for nano-technological application such as targeted drug-release capsules and microreactors. An important feature is that the polymersome membranes are often much thicker and more flexible than lipidic membranes. As a result, polymersomes have an improved stability with respect to outer and inner stimuli when compared to lipidic vesicles [7,8].

The basic physical mechanisms in cellular membrane fusion and fission are not well understood. Direct imaging of these phenomena is hindered, due to the small time and length scales involved. Moreover, cellular membranes generally consist of a wide variety of compounds. It is rather unknown what specific influence the abundant ones have on the membrane dynamics. However, there is some understanding that the pathways in many biological membranes are essentially lipidic in nature [5,6].

A direct consequence of this finding is that synthetic polymersomes and membranes may serve as a scaffold for the more complex biological systems, in a reductionist approach. The experimental and theoretical study of these synthetic polymersomes systems is therefore of great importance, and may eventually lead to a better understanding of the fundamentals of morphological processes in biological systems. Here, we focus on one particular class of molecules, the class of short amphiphilic molecules. The amphiphilic nature of synthetic or biological molecules is defined by its architecture, which consists of a hydrophobic and a hydrophilic (or, more general, a solphophobic and a solphophilic) part. When added to solvent, amphiphilic molecules align according to well-defined patterns and give rise to pluriform aggregates. The morphology of the

*Corresponding author. Email: a.sevink@chem.leidenuniv.nl

Molecular Simulation
ISSN 0892-7022 print/ISSN 1029-0435 online © 2007 Taylor & Francis
http://www.tandf.co.uk/journals
DOI: 10.1080/08927020601133391

aggregates is determined by the amphiphilic molecular architecture as well as the nature of the solvent. Scanning electron microscopy and scattering methods have revealed various morphologies: spherical micelles, micellar rods, bilayers, vesicles and inverted aggregates [7].

Self-organisation of amphiphilic molecules into membranes and vesicles is long seen as a complex interplay between kinetic and thermodynamic factors [1]. While the thermodynamic factor is well studied [4], the kinetic factor is subject to ongoing debate [2,3]. For lipids it was very recently decisively concluded that the spontaneous formation of vesicles is a kinetic rather than thermodynamic controlled process [2,3]. For polymeric vesicles it was suggested that they can be thermodynamically-stable rather then metastable, exemplary of the fact that the situation for block copolymer vesicles is far less clear.

Recently, much effort has been devoted to the analysis of vesicle formation [9–16] and fusion [17–22] by computer simulation. It should be noted that, especially in the fusion studies, the observed phenomena suffer from uncertainty due to the particular constraints (imposed stresses or enforced bilayer contacts) adapted in the different modeling approaches in order to initiate the fusion process. We argued previously that large-scale simulation, where multiple vesicle formation and fusion can be observed, is essential for the description of the evolution of a system with many metastable states. Modern supercomputers do not allow achieving this result with particle-based methods. Particle-based methods (both dynamical and Monte Carlo) have been able to simulate some separate steps of vesicle formation and evolution, but the time ranges and system sizes accessible by the methods are still far beyond those needed to realistically model experimental situations [8,23]. In particular, the simulation of a complete pathway from a homogeneous molecule mixture to vesicle fusion with all distinctive steps in one computer run is not accessible by these methods. The most advanced are aimed at modeling isolated events; they are able to describe the dynamics of one or at most two small vesicles in a simulation volume. Coarse-grained field methods, allowing for the simulation of larger volumes, are promising solutions. Indeed, a self-consistent field theory (SCFT) was applied to study vesicles and vesicular aggregates in two-dimensions (2D) [24] and three-dimensions (3D) [25]. However, both studies [24,25] do not allow for the investigation of actual kinetic pathways of vesicle formation.

Previously [26], we reported the results of large-scale 3D dynamic SCFT computer simulations of hierarchical self-assembly of polymeric amphiphiles, following the pathways from a complete mixture of molecules to the formation of large colonies of complex vesicles (like uni- and multi-layered vesicles, toroids, helicoids, etc), sometimes via fusion of smaller ones. Our method combines thermodynamics and kinetics, by minimizing a free energy for an ensemble of model molecules following the dynamics of the coarse-grained amphiphile density distributions, which effectively averages the movement of individual molecules. The results offered evidence that many complex vesicles can be thermodynamically-metastable structures. The vesicular shape is very diverse, and sensitive to a complex interplay of two kinetic processes: macro-phase separation of amphiphiles from solvent, and micro-phase separation between amphiphilic molecular blocks.

In the present contribution, we elaborate on the results of our previous article [26]. In particular, we consider the situation where part of the kinetic pathway, the macrophase separation of amphiphiles from solvent, is trespassed. To this aim, we use the same systems as in our earlier work [26] and investigate pattern formation in relatively small amphiphilic droplets immersed in solvent. This situation, where the initial macrophase separation structure is given, allows us to study the relation between macro- and micro-structure even more extensively. Initially, the amphiphiles are homogeneously distributed within this droplet. With time, the solphophilic and solphophobic parts of the molecules microphase separate. One may consider several experimental methods for generating these initially homogeneous droplets, for example, by dispersing insoluble molecules through sonification or through techniques developed for inktjet printing. Consequently, the simulation results have value by themselves as well.

One could be tempted to compare our results to the structures obtained in other types of confinement. For instance, very recently there has been much attention for block copolymer self-assembly in nanopores, both experimentally [27–31] and computationally [27,32–38], when the block copolymer is confined in an cylindrical tube with solid walls. In these nanopores, several intriguing non-bulk structures were observed and calculated for varying surface field and cylinder radius. Although these systems may at first glance look very similar, there is a crucial difference and we cannot directly use the nanopore results as a reference. In physically-confined environments, i.e. nanopores, the molecular packing is determined by interfacial interactions, symmetry breaking, structural frustration and confinement-induced entropy loss. In our microdroplets the confinement is soft, and the droplet as a whole may deform to balance the different entropic and enthalpic contributions to the free energy; the structure can thus (partially) avoid the entropy loss and frustration. In our previous work, we showed that this leads to surface topography that is often that of small valleys, ridges and bumps, reflecting the underlying morphology, very much like earths topography is an image of deeper events [41]. Moreover, confinement in a sphere differs from that in a cylinder, since the structures have to adapt to two principle curvatures (instead of one) as well as the natural domain distances. Physical confinement in a sphere has not been considered computationally at all, except for a lamella-forming system and a single sphere radius [33]. For this case, onion structures were found both in physical confinement [33] and in microdroplets (see results section). In Ref. [39] the interested reader can find a recent review of several types of templated self-assembly. To our

knowledge, this paper also includes the only known experimental record of microdroplet structures (see figure 12 in that article). Onion structures are indeed formed for short symmetric diblock copolymers upon confinement in a microdroplet [41]. For much larger molecular weights a structure that is believed to be a "plumbers nightmare" is observed: a chaotic bicontinuous (Bic) structure. When the diblock is chosen non-symmetric (in bulk: a double diamond structure), the structure in the microdroplet is that of a distorted network, very much similar to figure 1c,d in Ref. [41]. We note that our amphiphiles are short, and that the general features of the structures in our computational studies, here and in Ref. [41], are supported by these experimental findings. To be complete, there are also a number of studies on the packing of microspheres upon confinement in a solvent droplet (see for instance Ref. [40]). Although packing is also an issue here, the situation in our system is substantially different, since there is an inherent microdomain packing frustration due to the connectivity of the different diblock copolymer blocks that is absent in the microsphere system.

The system in Fraaije *et al.* [41] was chosen to model a PEO–PPO diblock, with relatively weak energetic interactions allowing for the uptake of a reasonably amount of solvent in the hydrophilic PEO-rich part of the microstructure. The free energy was that for an *nVT* ensemble, and accordingly we did not calculate the global equilibrium in an open system, but rather a local equilibrium morphology of an isolated droplet. The situation is analogous to that of the classic study of the shape of an isolated lipid vesicle, when interactions between vesicles are less relevant. With the selected values of the Flory–Huggins (FH) parameters and solvophobic/philic block fractions, the polymers were all insoluble, hence the deformations of the droplets was at constant mass of polymer. As a result, in most cases the stable microstructure in the droplet was that of shells centred around the midpoint of the droplet. The shell structures themselves are restricted 2D analogs of the 3D bulk structures for the considered block ratios; in this context a space filling Bic structure is analogous to a perforated lamellae (PL) phase. Only due to the fact that the PL shell has to close upon itself, the strict hexagonal arrangement of the pores is replaced by a mixed pore pattern of pentagons, hexagons and septagons. In all case, the number of shells was a direct consequence of the initial radius of the droplet. Here, the situation is different as all interaction parameters are much higher than in the previous system [41]. As a result, the solvent is less likely to penetrate into either of the amphiphilic blocks, and swelling through the uptake of solvent is suppressed. The microstructures (in bulk: lamellar, Bic or cylindrical phases) have to respond to the imposed spherical confinement in alternative ways. This may lead to frustration, however, the confinement is soft: the droplet can change its shape in accordance to the thermodynamic driving forces present in- and out-side the droplet. We will relate the phase behavior of these isolated droplets to vesicle formation that results from co-operative macro- and micro-phase separation [26].

2. Method

We give a short outline of the theory used in the calculations; for more details see Ref. [45–47] and references therein. We model the pattern formation that occurs when a block copolymer melt or solution is brought into a state where the chemically different blocks phase separate on a mesoscopic level (1–1000 nm). In our model, an amphiphilic molecule is represented by a short Gaussian chain $A_{N_A}B_{N_B}$, consisting of $N_a = N_A + N_B$ beads. Each bead (A or B) typically represents a number of chemical monomers. Differences in monomers gives rise to different bead species. Similarly to the approach in Ref. [48] a collection of solvent molecules is represented by a single bead S ($N_s = 1$). The 3D volume used in the calculations (periodic boundary conditions apply) is denoted by V^{system}, and contains a total of $n = n_a + n_s$ Gaussian chains. Here, n_a is the number of amphiphile chains and n_s the number of solvent beads. The inter-chain interactions are incorporated via a mean field with interaction strength controlled by the FH parameters χ_{IJ}. In line with our earlier work [46,47] the interactions are specified by the parameters ε^0_{IJ} (in kJ/mol) [48], which are directly related to the dimensionless FH parameters by $\chi_{IJ} = \varepsilon^0_{IJ}/n_A k_B T$ (with n_A Avogadro's number, k_B the Boltzmann constant and $T = 300$ the temperature in Kelvin). We note that the choice for ε^0_{IJ} in kJ/mol is for our convenience only; in order to relate given values to the more general FH parameters, ε^0_{IJ} should be recalculated in J/mol in order to obtain the correct dimensionality.

The microstructure patterns are described by coarse-grained variables, which are the density fields $\rho_I(\mathbf{r})$ of the different species $I \in \{A, B, S\}$. Given these density fields a free energy functional $F[\rho]$ can be defined as follows [42,45–47]

$$F[\rho] = -kT \ln \frac{\Phi^{n_a}\Phi^{n_s}}{n_a! n_s!} - \sum_I \int_{V^{\text{system}}} U_I(\mathbf{r})\rho_I(\mathbf{r}) \mathrm{d}r + F^{\text{nid}}[\rho]. \quad (1)$$

Here Φ is the partition function for the ideal Gaussian chain in external fields U_I, and F^{nid} is the contribution due to the non-ideal mean-field interactions. The external potentials U_I and the density fields ρ_I are bijectively related in a self-consistent way via a density functional for Gaussian chains.

Several methods can be employed to find the minimum of free energy (1) and equilibrium density fields $\rho_I(\mathbf{r})$. They can roughly be divided into *static* and *dynamic* methods, although a number of hybrids exist which are generally referred to as quasi-dynamic methods (for instance [49]). A rather complete and recent review is given in Ref. [50]. In this article, we use the same dynamic

scheme as used previously [26]. An advantage of this scheme is that it intrinsically considers dynamic pathways towards a free energy minimum, including visits to long-living metastable states. In this sense, the model can be seen to mimic the experimental reality when compared to static schemes, which are optimizations, based upon mathematical arguments. The thermodynamic forces driving the pattern formation in time are the gradients of the chemical potential $\mu_I(r) = \delta F/\delta\rho_I$ and the time behavior of the density field is therefore given by the following Langevin equation [45,48]

$$\frac{\partial\rho_I}{\partial t} = M_I\nabla\cdot\rho_I\nabla\mu_I + \eta_I \tag{2}$$

where M_{I} is a constant mobility for bead I and $\eta_{\mathrm{I}}(\mathbf{r})$ is a noise field, distributed according to the fluctuation–dissipation theorem.

The starting configuration is a matter of choice. The numerical scheme explicitly considers the external potential fields U_{A}, U_{B} and U_{S} instead of the density fields ρ_{A}, ρ_{B} and ρ_{S}. Concentrating on the amphiphilic chain (the expressions for the solvent can easily be deduced from the more general expressions) an explicit (bijective) relation to the densities is given by the density functional [46]

$$\begin{aligned}\rho_{\mathrm{A}}(\{U\})(\mathbf{r}) &= \frac{n_{\mathrm{a}}}{\mathcal{N}}\sum_{s=1}^{N_{\mathrm{A}}}\int_{V^{N_{\mathrm{a}}}}\psi_{\mathrm{a}}\delta(\mathbf{r}-\mathbf{R}_s)\mathrm{d}\mathbf{R}_1\ldots\mathrm{d}\mathbf{R}_{N_{\mathrm{a}}}\\ \rho_{\mathrm{B}}(\{U\})(\mathbf{r}) &= \frac{n_{\mathrm{a}}}{\mathcal{N}}\sum_{s=N_{\mathrm{A}}+1}^{N_{\mathrm{a}}}\int_{V^{N_{\mathrm{a}}}}\psi_{\mathrm{a}}\delta(\mathbf{r}-\mathbf{R}_s)\mathrm{d}\mathbf{R}_1\ldots\mathrm{d}\mathbf{R}_{N_{\mathrm{a}}}\end{aligned} \tag{3}$$

with $\mathcal{N} = \Lambda^{3N_{\mathrm{a}}}$ a normalization factor and

$$\psi_{\mathrm{a}} = \frac{1}{\Phi_{\mathrm{a}}}\mathrm{e}^{-\beta\left[H^{\mathrm{G}}(\mathbf{R})+\sum_{s=1}^{N_{\mathrm{a}}}U_s(\mathbf{R}_s)\right]} \tag{4}$$

the single-chain distribution function, and

$$\Phi_{\mathrm{a}} = \frac{1}{\mathcal{N}}\int_{V^N}\mathrm{e}^{-\beta\left[H^{\mathrm{G}}(\mathbf{R})+\sum_{s=1}^{N_{\mathrm{a}}}U_s(R_s)\right]}\mathrm{d}\mathbf{R}_1\ldots\mathrm{d}\mathbf{R}_{N_{\mathrm{a}}} \tag{5}$$

the single chain partition function. Here, the Hamiltonian $H^{\mathrm{G}}(\mathbf{R}) = \mathcal{N}_1\sum_{s=2}^{N_{\mathrm{a}}}(\mathbf{R}_s-\mathbf{R}_{s-1})^2$ ($\mathcal{N}_1 = 3\beta^{-1}/2a^2$, a the bond length) is the standard Hamiltonian of a Gaussian chain. This complicated path integral can be evaluated via a recursive scheme

$$\begin{aligned}\rho_{\mathrm{A}}(\{U\})(\mathbf{r}) &= \frac{n_{\mathrm{a}}}{\mathcal{N}\Phi}\sum_{s=1}^{N_{\mathrm{A}}}G_s(\mathbf{r})\sigma(G^i_{s+1})(\mathbf{r}),\\ \rho_{\mathrm{B}}(\{U\})(\mathbf{r}) &= \frac{n_{\mathrm{a}}}{\mathcal{N}\Phi}\sum_{s=N_{\mathrm{A}}+1}^{N_{\mathrm{a}}}G_s(\mathbf{r})\sigma(G^i_{s+1})(\mathbf{r})\end{aligned} \tag{6}$$

where the functions G and G^i are given by recursive relations $G_s(\mathbf{r}) = \mathrm{e}^{-\beta U_s(\mathbf{r})}\sigma(G_{s-1})(\mathbf{r})$ and $G^i_s(\mathbf{r}) = \mathrm{e}^{-\beta U_s(\mathbf{r})}\sigma(G^i_{s+1})(\mathbf{r})$, subjected to the boundary conditions $G_0(\mathbf{r}) = G^i_{N_{\mathrm{a}}+1}(\mathbf{r}) = 1$. The functional σ is a integral operator with a Gaussian kernel defined by

$$\sigma(f)(\mathbf{r}) = \left(\frac{3}{2\pi a}\right)^{3/2}\int_V \mathrm{e}^{(3/2a^2)(\mathbf{r}-\mathbf{r}')^2}f(\mathbf{r}')\mathrm{d}\mathbf{r}'. \tag{7}$$

It is normalized such that $\sigma(f)(\mathbf{r}) = 1$ for a function $f(\mathbf{r}) = 1\forall\mathbf{r}\in V^{\mathrm{system}}$.

We find it convenient to introduce dimensionless concentration fields $\theta(\mathbf{r}) = \nu\rho(\mathbf{r})$, with ν the physical volume of the problem (if we choose ν to be the volume of one bead, $0\le\theta(\mathbf{r})\le 1$) For the limiting case that $\forall s\in\{1,\ldots,N_{\mathrm{a}}\}U_s(\mathbf{r}) = 0$ for all $\mathbf{r}\in V^{\mathrm{system}}$ the configuration of the chain is that of an unperturbed Gaussian chain and $\theta_I(\mathbf{r}) = \nu\rho_I(\mathbf{r}) = \nu nN_I/\mathcal{N}\Phi = N_I/N_{\mathrm{a}} = c_I$. The concentration c_I is the volume-average of the dimensionless concentration fields $\theta_I(I\in\{\mathrm{A},\mathrm{B}\})$, and constant for incompressible systems, $\sum_{I=\mathrm{A,B}}c_I = c_{\mathrm{a}}$ (c_{a} is the total concentration of amphiphiles in the system V^{system}). In the other extremum that $\forall s\in\{1,\ldots,N_{\mathrm{a}}\}U_s(\mathbf{r})\to\infty$ in a volume $V^{\infty}\subset V^{\mathrm{system}}$, the density $\theta_I(\mathbf{r}) = \nu\rho_I(\mathbf{r}) = 0$ for all $\mathbf{r}\in V^{\infty}$.

In most calculations, the starting configuration is that of a fully mixed system, $\theta_I(\mathbf{r},t=0) = c_I = N_I/N_{\mathrm{a}}$ (or, similarly, $\forall s\in\{1,\ldots,N_{\mathrm{a}}\}U_{\mathrm{s}} = 0$). In the case that a calculation is started from another spatial distribution of material, for instance a droplet of polymer in a solvent, the input fields $U_I(\mathbf{r},t=0)$ (or alternatively $\theta_I(\mathbf{r},t=0)$) are generated by iterative minimization of the expression

$$\sum_{I=A,B,S}|\theta_I(\{U\})(\mathbf{r}) - \theta_I(\mathbf{r},t=0)| \tag{8}$$

by a steepest descent scheme, prior to the application of the dynamic scheme of equation (2). The initial values are usually taken as $U_{\mathrm{s}}(\mathbf{r}) = 0\forall s\in\{1,\ldots,N_{\mathrm{a}}\}$ (and consequently $\theta_I[U_I=0](\mathbf{r}) = c_I$), and $U_{\mathrm{S}}(\mathbf{r}) = 0(\theta_{\mathrm{S}}(\mathbf{r}) = c_{\mathrm{s}})$. An update of the external potentials is accepted when the L_2 norm is smaller than some preset value $\delta << 1$. For arbitrary input fields, for example, unphysical step profiles, the difference will never vanish completely. However, for a small but large enough δ a very "natural" interface is automatically generated in this way.

3. Minkowski functionals

Determining the underlying fundamental mechanisms in structure transformation is a difficult task. The huge scales in space and time covered by our (parallel implemented) simulation technique, hampers us from grasping the important features from imaging the 4D data alone. To give an idea: for the intermediate size systems considered in this article, the amount of data is as large as $64\times64\times64 = 262144$ double-precision (8 bytes) spatial data times 600 (writing spatial information every 50 time steps for a total of 30,000 time steps), resulting in a total amount of data for each simulation of almost 1.3 GB. Modern integral-geometry morphological image analysis provides the tool to assign numbers to the shape and connectivity of patterns

formed by pixels of 3D images, by means of additive image functionals. An example of such additive image functionals are the Minkowski functionals, that describe the morphological information contained in an image by numbers that are proportional to very simple geometrical and topological quantities: the volume V, the surface area S, the mean curvature H, and the Euler characteristic χ_E. The latter is related to the (integrated) Gaussian curvature, and can be understood as the number of connected components minus the number of tunnels (holes) plus the number of cavities. For instance, it is 1 for a solid sphere, 2 for a hollow sphere, 0 for a torus and -1 for an ∞-shape which has 2 holes. For simple AB and ABA systems in the absence of solvent, the amount of amenable mesostructures is limited to spherical, cylindrical, Bic or lamellar morphologies, and a few very simple rules for the interpretation of structures drop out: a very positive Euler characteristic can be interpreted as a majority of spherical or (compact) cylindrical structures, a very negative Euler characteristic as highly connected structures with many tunnels. From the Euler characteristic it is impossible to distinguish between spheres and cylinders of finite length. Due to the additivity, we can use this knowledge for the determination of the topology of the majority part of the local structures from the Euler characteristic. For the amphiphiles/solvent mixtures considered here, the situation is far less straightforward, but the Minkowski functionals can still serve as an identification tool for pattern formation mechanisms [26,44].

4. Order parameter

Apart from the geometrical and topological characterization of the simulated structures, we use the segregation parameter $P_I = (1/V \int_V \mathrm{d}\mathbf{r}\,\theta_I(\mathbf{r})^2) - (\bar{\theta}I)^2$. $P_I = (1/V \int_V \mathrm{d}\mathbf{r}\,\theta_I(\mathbf{r})^2) - (\bar{\theta}_I)^2$. $(I \in \{A, B, S\})$ to characterize the degree of phase separation. Here $\bar{}$ defines the spatial average of a function. In a homogeneous system $P_\mathrm{I} = 0$, while in a totally segregated system $P_I^{\max} = \bar{\theta}_I - (\bar{\theta}_I)^2$.

5. Parametrization

5.1 Systems choice

The choice of chain architecture and interaction parameters was discussed earlier in detail [26]; for completeness we repeat it shortly. The interaction parameters are the same as in the large scale simulations in that article, $\varepsilon^0_{AB} = 12$, $\varepsilon^0_{AS} = 16$ and $\varepsilon^0_{BS} = 7$ (all in kJ/mol), which were determined for small scale simulations of a A_2B_3/S system (20/80 vol%) as the onset of the region where platelets are formed. The formation of platelets is a prerequisite for vesicle formation. In correspondence with the earlier work [26] we have only varied the length N_B of the solphophilic part of the $A_2B_{N_B}$ chain (from 2 to 6 beads or statistical units). In many biological membranes the solphophobic (tail) part of the molecules is larger than the solphophilic part (head). We varied the length of the relative solphophilic (head) block instead, as we had a specific interest in the fundamentals of geometrically and topologically complex experimental polymeric vesicular structures, that originate from a frustration of the (inner) solphophobic block, like the exotic structures observed by the Eisenberg group [43].

5.2 Starting conditions

All simulations are started from a homogeneous amphiphilic droplet in solvent. For the general case of d droplets of radius $R^{\,\mathrm{d}}$ and centre $\mathbf{r}^{\mathrm{d}} = (x_0^{\mathrm{d}}, y_0^{\mathrm{d}}, z_0^{\mathrm{d}})$, we found it advantageous to choose input fields that have a step profile: $\theta_I(\mathbf{r}, t = 0) = N_I/N_\mathrm{a}$ for $\left|\mathbf{r} - \mathbf{r}^{\mathrm{d}}\right| \leq R$ and $\theta_I(\mathbf{r}, t = 0) = 0$ for $\left|\mathbf{r} - \mathbf{r}^{\mathrm{d}}\right| > R (I \in \{A, B\})$. At the positions $\mathbf{r}$ that are in intersections of different droplets, the local field values are scaled to 1. The input solvent field $\theta_\mathrm{S}(\mathbf{r}, t = 0)$ is related to the input polymer fields by $\theta_\mathrm{S}(\mathbf{r}, t = 0) = 1 - \sum_{I=A,B} \theta_I(\mathbf{r}, t = 0)$, assuring incompressibility. The simulation volumes (periodic boundary conditions apply) are chosen such that the droplet is at least $R^{\,\mathrm{d}}$ away from the simulation volume boundary. The free energy model is that for an nVT ensemble, and accordingly we do not calculate the global equilibrium in an open system, but rather local equilibrium morphology of an isolated droplet. The situation is analogous to that of the classic study of the shape of an isolated lipid vesicle, when interactions between vesicles are less relevant. With the selected values of the FH parameters, and N_A and N_B, the amphiphiles are all insoluble; hence, the deformations of the droplets are at constant mass of material. As a consequence, we take $h = N_\mathrm{A}/N_\mathrm{a}$ as the threshold value in the calculation of the Minkowski functionals (unless mentioned different explicitly).

6. Results and discussion

6.1 Small single droplets

We performed five simulations for a small initial droplet radius, $R^{\,1} = 8$ grid points, and different chain architectures, A_2B_j $(j = 2, \ldots, 6)$. The solvent and amphiphile concentrations are $c_\mathrm{s} = 0.9356$ and $c_\mathrm{a} = 0.0644$, respectively, and the amphiphiles are homogeneously distributed inside the droplet at time step $= 0$. Recalculated to the large simulation volumes of our previous study [26], the size of this droplet is approximately 0.4 vol%, and it is at the lower end of the cluster sizes obtained in this previous work.

In figure 1a the final shape of the droplets is shown. The solvent/amphiphile interface is defined as the locations where $\theta_\mathrm{S} = 0.5$. Figure 1b is the corresponding microstructure of the solphophobic A-part of the amphiphile (an isosurface for $\theta_\mathrm{A}(\mathbf{r}) = 0.5$). All simulations were stopped at a point where the structure was

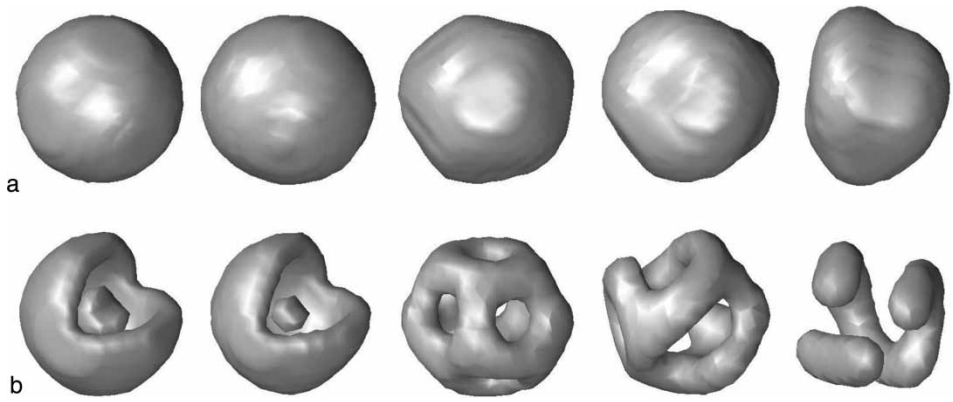

Figure 1. Final structures for: (a) the droplet (isosurface for $\theta_S = 0.5$), and (b) hydrophobic component (isosurface $\theta_A = 0.5$), at different stages and for different length j of the hydrophilic block: (from left to right) $j = 2$ (time step 10,000), $j = 3$ (time step 40,000), $j = 4$ (time step 40,000), $j = 5$ (time step 40,000) and $j = 6$ (time step 40,000). The initial radius of the droplet was eight grid points.

frozen in, which is monitored by the change in the free energy and the Minkowski functionals (the evolution of these four quantities is shown in figure 2). For all systems, the free energy (not shown here) falls-off to a constant value.

From figure 1a,b, we see that the initial perfectly spherical droplets remain relatively undeformed for $j = 2$ and 3, while for $j = 4$–6 the droplet shape adapts to the underlying non-spherical microstructures. For $j = 2$–3 the hydrophobic A blocks phase-separate into an union

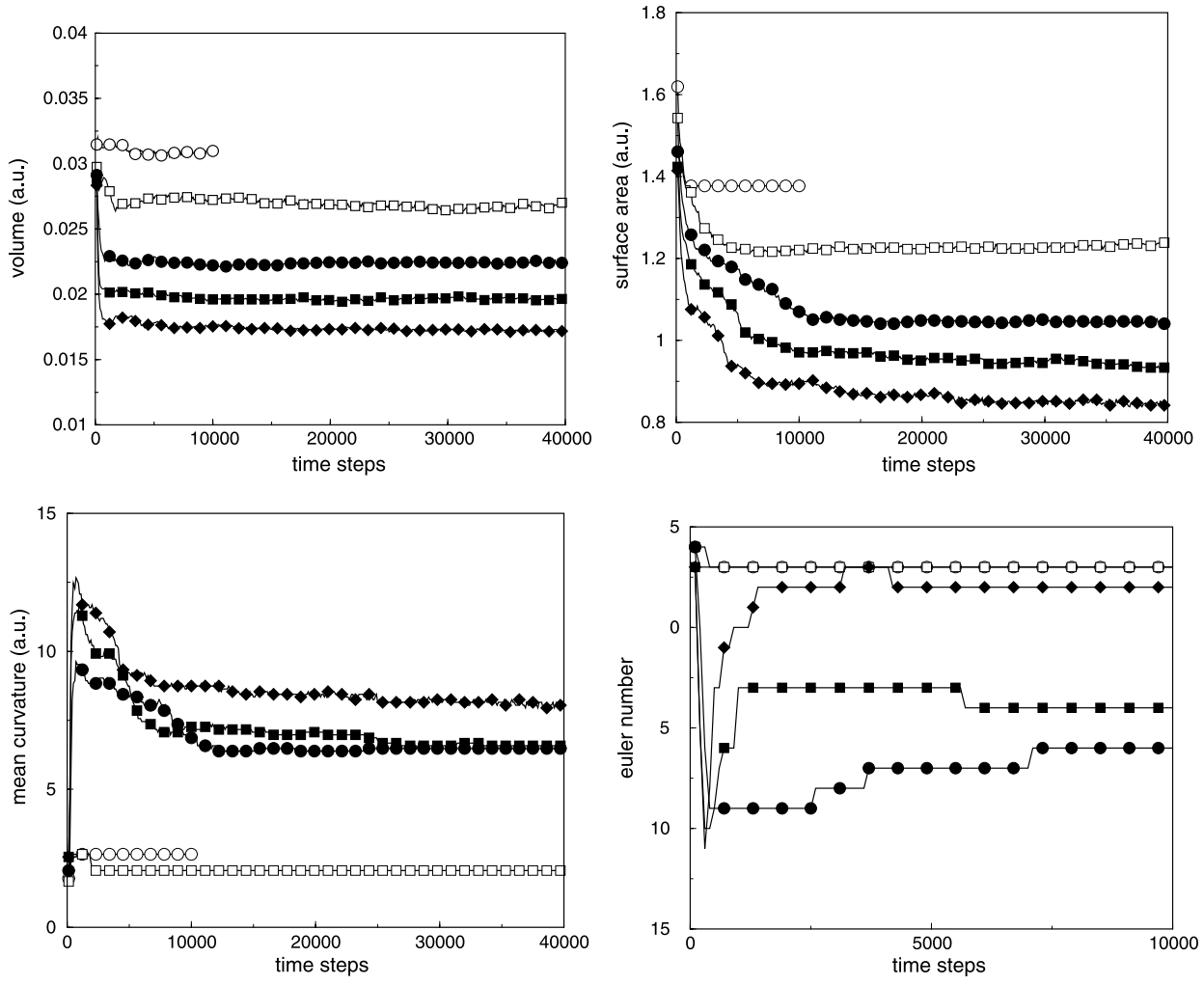

Figure 2. The time evolution of the Minkowski functionals for the small droplet microstructures of the solphophobic A-block (the threshold value was taken equal to $h = N_A/N_a$). The symbols denote: $j = 2$ (○), $j = 3$ (□), $j = 4$ (●), $j = 5$ (■) and $j = 6$ (◆).

structure. For longer hydrophilic blocks, the shape resembles the cage-like bucky-ball structure [41] ($j = 4$), a defected version of a cage ($j = 5$) where some of the perforations widen and the overall structure is an intermediate between a PL and a cylindrical structure, and two cylinders of finite size ($j = 6$), one of which is twisted into a peculiar shape.

For further analysis, we first concentrate on the interesting features of the Minkowski functionals for the $\theta_A(\mathbf{r})$ field (figure 2). The volume starts from relatively high values and drops off to values that fluctuate around a constant value around time step 5000 for all j. The relatively high volume values at the beginning may seem strange, but the origin is simple. As we start from a homogeneous droplet with relatively high χ_{AB}, the initial situation is that of a fast microphase-separating droplet. Since this process takes place all over the droplet simultaneously there is a competition between the emerging microstructure and the tendency to avoid energetically unfavored contacts between A blocks and solvent beads. As a result, the system has to redistribute matter along the way. The response is a contraction of the outer A blocks towards the center of the droplet and rearrangement in the center to compensate for this effect. As a result, there is a flux of material, and the amount of matter above the average concentration is slightly larger than below, resulting in an increased volume above the threshold (which is the average concentration) at the first stages. This feature is indeed present for all j. The surface area decreases mostly monotonically for all $j = 2, \ldots, 6$ and saturates at a constant value; this value is highest for $j = 2$ and lowest for $j = 6$. The mean curvature increases at the first stages and then mostly descents for all j. An interesting observation is that the mean curvature for the symmetric amphiphile ($j = 2$) is larger at the final stage than the one for the slightly asymmetric amphiphile ($j = 3$); one may conclude that the structure for $j = 2$ is completely trapped due to the imposed spherical droplet constraint. The evolution of the Euler characteristic (which is related to the Gaussian curvature) is relatively dull. For $j = 2$, 3 and 6 χ_E is positive, due to

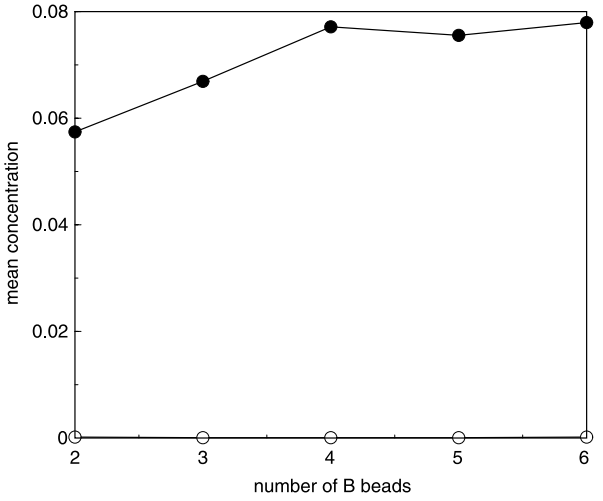

Figure 3. Solvent concentration inside the droplets of figure 1 (●) and A-block concentration outside the droplet (○). Both concentrations are dimensionless; the solvent/amphiphile interface is considered at $\theta_S(\mathbf{r}) = 0.5$.

structure of concentric shells ($j = 2$, 3) and two short cylinders ($j = 6$; topologically seen as spheres, and therefore each $\chi_E = 1$). Apparently the decrease in surface area and mean curvature for $j = 3$ is obtained without a change of the overall topology. The steps in the evolution of the cage-like structures ($j = 4$, 5) are due to the fusion or fission of perforations, which is apparently a rather slow mechanism.

Finally, we consider the segregation parameters (not shown here) and the concentration of the solvent inside the droplet (figure 3). For all j, the amount of amphiphile dissolved in the solvent is negligible (< 0.01 vol%). The segregation parameters P_A, P_B increase monotonously with increasing time, and level off to a constant value very early on in the process, an indication that most of the structural rearrangements are not accompanied by (local) mixing. Only P_S is decreasing during the whole evolution, indicative of solvent being slowly taken up by the droplet. Indeed, figure 3 shows that more than 5 vol% of solvent

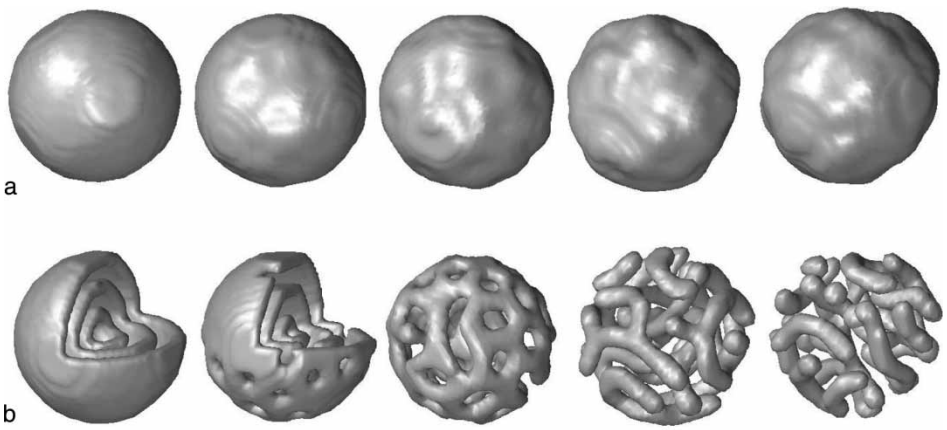

Figure 4. Final structures for: (a) the droplet (isosurface for $\theta_S = 0.5$), and (b) hydrophobic component (isosurface $\theta_A = 0.5$), at different stages and for different length j of the hydrophilic block: (from left to right) $j = 2$ (time step 10,000), $j = 3$ (time step 40,000), $j = 4$ (time step 40,000), $j = 5$ (time step 40,000) and $j = 6$ (time step 40,000). The initial radius of the droplet was 16 grid points.

is present, and that more solvent is taken up for larger j. This is not a surprise, as in that case the concentration of B-blocks (the solphophilic blocks) is considerable larger.

6.2 Larger single droplets

We also performed five simulations for a twice larger initial droplet radius, $R^1 = 16$ grid points, and different chain architectures, A_2B_j ($j = 2,\ldots,6$). The solvent and amphiphile concentrations are $c_s = 0.9349$ and $c_a = 0.0651$, respectively, and the amphiphiles are homogeneously distributed at time step = 0. Recalculated to the large simulation volumes of our previous study [26], the size of this droplet is approximately 3.5 vol%. This size is at the higher end of the cluster sizes obtained in the previous work. In figure 4a the final shape of the droplets is shown. Figure 4b is the corresponding microstructure of the solphophobic A-part of the amphiphile (an isosurface for $\theta_A(\mathbf{r}) = 0.5$). All simulations were stopped at a point where the structure was frozen in, which is monitored by the change in the free energy and the Minkowski functionals (the evolution of these four quantities is shown in figure 5).

From figure 4a,b, we see similar behavior: the initial perfectly spherical droplets remain relatively underformed for $j = 2$ and 3, while for $j = 4$–6 the droplet shape adapts to the underlying non-spherical microstructures. For $j = 2$–3 the hydrophobic A-blocks phase-separate into an union structure. The structure for $j = 2$ is completely isotropic and comparable to the one for $R^1 = 8$ grid points (but with more shells); for $j = 3$ a number of perforations appear. For longer hydrophilic blocks ($j = 4$), the shape again resembles the cage-like bucky-ball structure with many defects [41]. For $j = 5$ and 6 the structure is mostly cylindrical. When compared to the structures of [41] a shell-like organization is absent for chains with a longer hydrophilic block: much more isolated cylinders can be seen.

We again concentrate on the interesting features of the Minkowski functionals for the $\theta_A(\mathbf{r})$ field (figure 5). As the initial situation (homogeneous droplets) is the same apart from the size, we again observe the same phenomena in

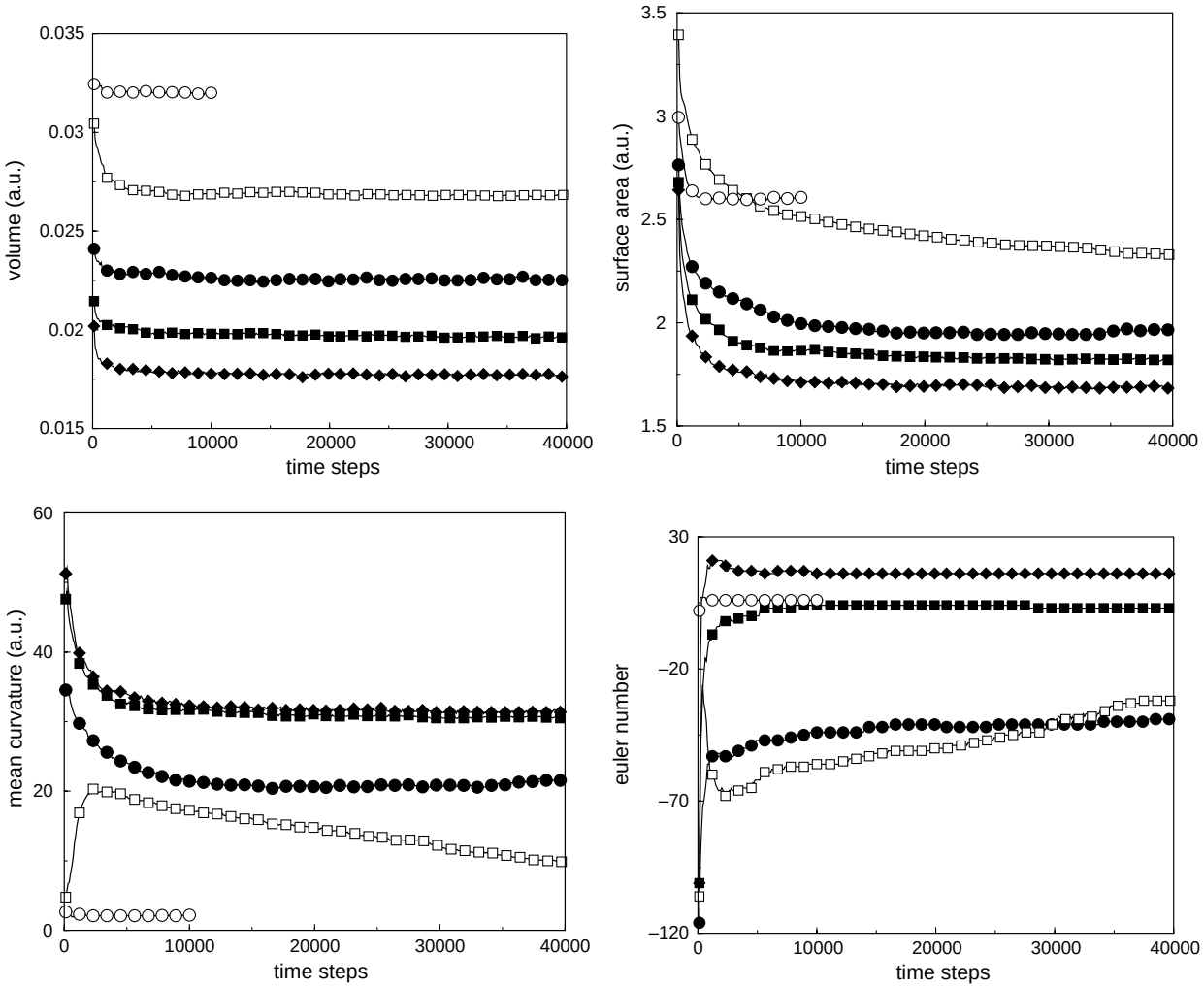

Figure 5. The time evolution of the Minkowski functionals for the large droplet microstructures of the solphophobic A-block (the threshold value was taken equal to $h = N_A/N_a$). The symbols denote: $j = 2$ (○), $j = 3$ (□), $j = 4$ (●), $j = 5$ (■) and $j = 6$ (◆).

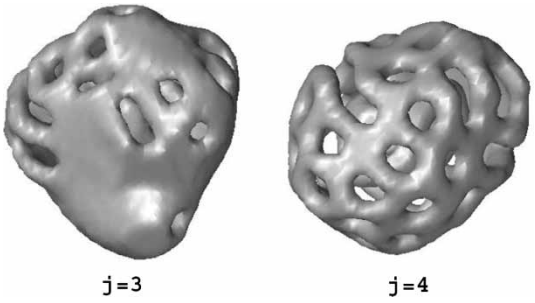

Figure 6. Final structures (time step 40,000) for the hydrophobic component (isosurface $\theta_A = 0.5$) for a more compressible system and $j = 3, 4$. The initial radius of the droplet was 16 grid points.

the evolution of the volume. The surface area is mostly decreasing for all j, except for small bumps. For the case where macro- and micro-phase separation are taking place at the same time, we have concluded [26] that the sphere–cylinder–platelet-vesicle transition is mainly curvature driven and that the surface tension should be small, which is always the case for any real surfactant system. Here, we observe that the mean curvature goes down monotonously for $j = 2, 5$ and 6, but increases first sharply for $j = 3, 4$ and then falls down monotonously. We claim that this increase is an effect of the high solvent concentration around the droplet that acts as a strong constraint on the solvent/amphiphile interface and against more thermodynamically favorable droplet deformation. As a test, we lowered the incompressibility parameter κ_H in equation (1), allowing the system more flexibility in adapting a non-spherical droplet morphology. The result is shown in figure 6. Indeed, the reduction of the mean curvature is accompanied by deformation of the droplet into another geometry. A closer look at the structure for $j = 3$ shows that it is very similar to the structure shown in figure 9c of Sevink *et al.* [26]. Coming back to the Euler characteristic of the original systems, we see that both the structures for $j = 3$ and 4 are cage-like (highly-connected, negative χ_E). The main difference between the structures for $j = 5$ and 6 is that the average size of the separate elements is larger for $j = 5$ (leading to a smaller, but positive, Euler number).

The segregation parameters (not shown here) and the concentration of the solvent inside the droplet (figure 7) are very similar to the ones in the previous section. The concentration of solvent in the droplet for $j = 3$ is relatively larger than for the small droplets. It is an indication that the formation of perforations is mediated by the presence of solvent.

6.3 Two large droplets

We also performed two simulations to investigate fusion phenomena. To this aim, we consider a combination of the two systems showing vesicle formation in the earlier work [26]. The starting configuration is that of two large droplet of radius $R^1 = 16$ grid points, each with a different composition: A_2B_2 or A_2B_3. Starting from the situation where the droplets are separated by solvent, we observe no

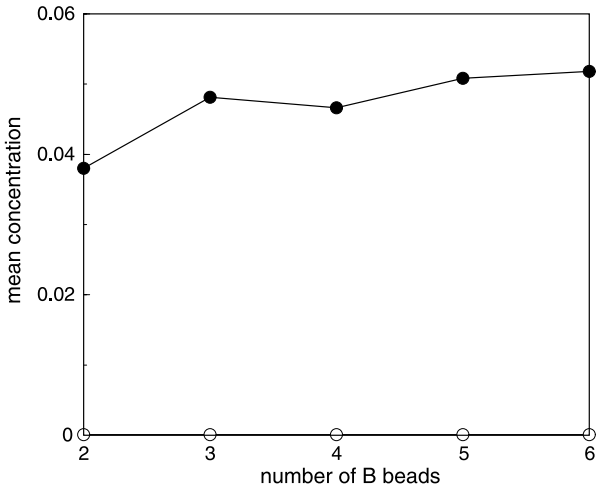

Figure 7. Solvent concentration inside the droplets of figure 4 (●) and A-block concentration outside the droplet (○). Both concentrations are dimensionless; the solvent/amphiphile interface is considered at $\theta_S(\mathbf{r}) = 0.5$.

fusion within the time scales considered in our simulations. The droplets micro-phase separate, but the microstructure is that of two separate droplets: there is no interaction between the droplets, most likely because the solvent/amphiphile interaction is too unfavorable. This finding is in agreement with experimental findings that the fusion rates of larger vesicles are almost negligible [2,3]. When the initial situation is such that the droplets partially overlap, a fusion process does take place. The details of this process are shown in figures 8 and 9. They show that the micro-phase separation is the fastest process (as expected), but that the A_2B_3 amphiphile redistributes itself asymmetrically over the original A_2B_2 droplet, thereby reducing the total solvent/amphiphile interface

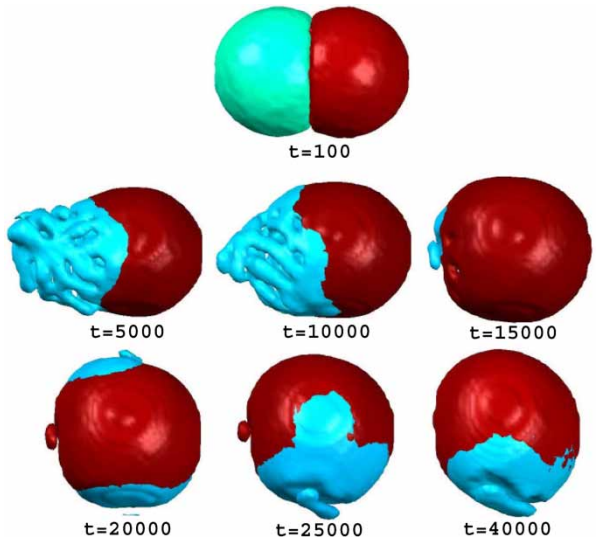

Figure 8. Structural evolution of two merging droplets (both isosurfaces for $\theta = 0.25$): blue, a component of A_2B_3, red, a component of A_2B_2 (from top to bottom, left to right) time step = 100, 5000, 10,000, 15,000, 20,000, 25,000 and 40,0000. The initial radius of the droplets was 16 grid points (colour in online version).

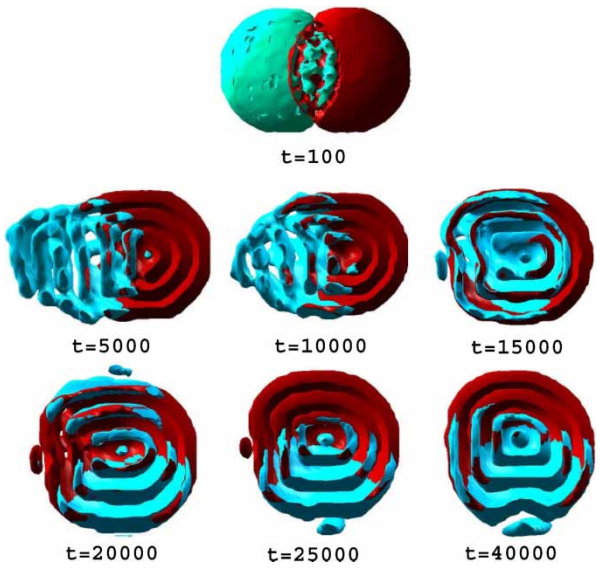

Figure 9. Details of figure 8. Part of the structures is not displayed, in order to show the inner structure.

dramatically. The end situation is that of a janus-like vesicle, where one part consists of a (half) concentric onion, and the other part is free to adapt its local curvature to the preferred curvature of the A_2B_3 amphiphile at hand. Comparing the Euler number and the mean curvature (figure 10) for both *A* blocks belonging to different amphiphiles we observe that they converge in time to matching values. This convergence is at the expense of the volume and surface area that shows asymmetric behavior: a decrease for one block goes to the expense of the other block. This observation corroborates our earlier conclusion that most of the processes are curvature driven.

7. Conclusion

We have used dynamic self consistent field theory and preset macro-phase separated structures (droplets of amphiphiles) to investigate in detail the different factors in vesicle formation. Changing the size and number of the initial droplets we observe several dependencies. For

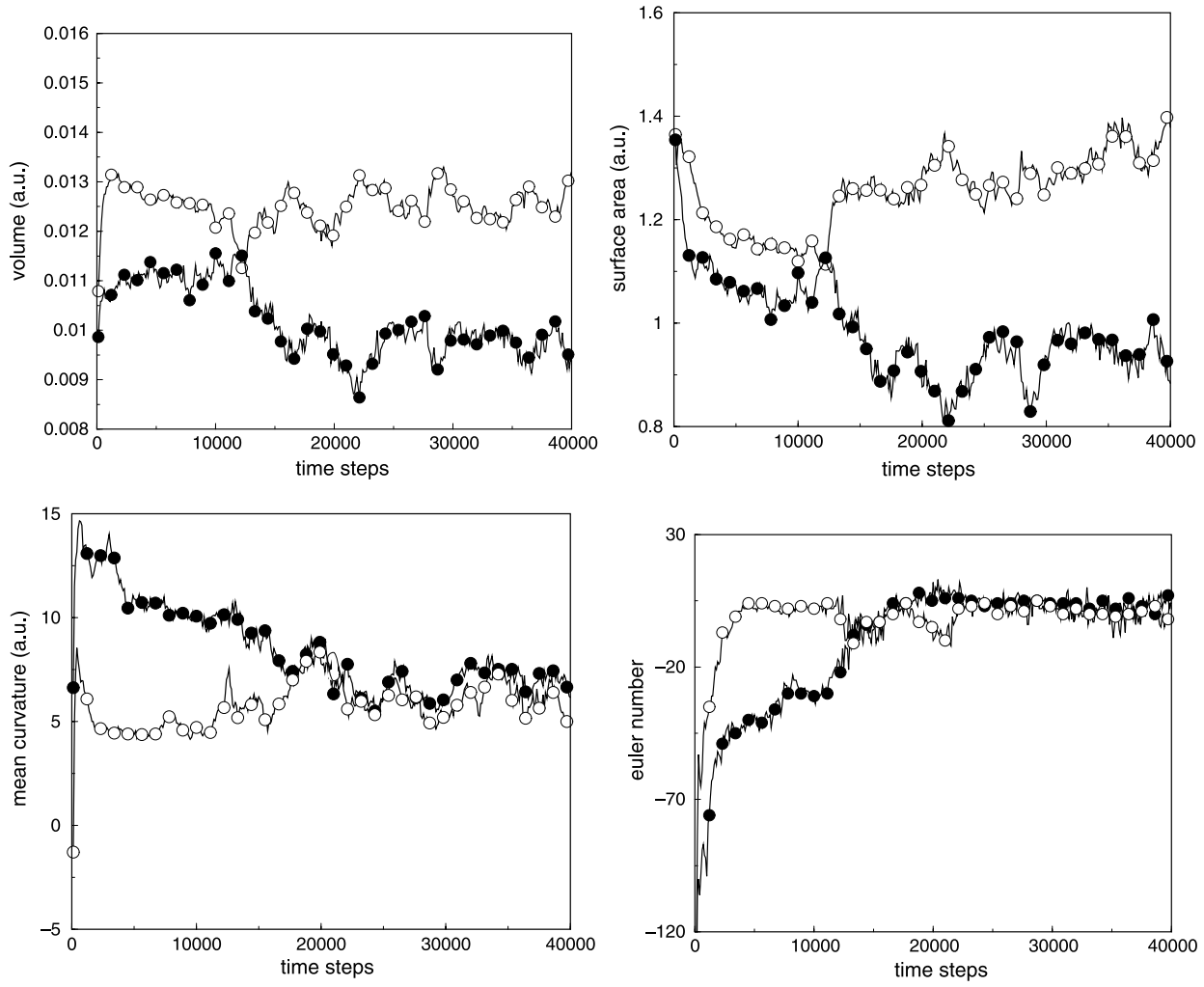

Figure 10. The time evolution of the Minkowski functionals for both solphophobic A-blocks (the threshold value was taken equal to $h = N_A/N_a$): A_2B_2 (○) and A_2B_3 (●).

symmetric systems ($j = 2$), we conclude that once an onion is formed it is the most stable structure; for very small droplets our results suggest, however, that the onion structure is frustrated. This observation is in qualitative agreement with the only experimental study of microdroplets [39], were the microdroplet structure of symmetric diblock copolymer was found to depend crucially on the ratio d of droplet radius and polymer molecular length. Two different structures were observed: an onion structure for large or intermediate d and a chaotic Bic structure when d becomes small. Here, we observe frustration for the smallest d. However, we can only consider a limited range of d values, since we restricted ourselves to the same short amphiphiles as in Ref. [26]. The existence of an actual structural transition for decreasing d will be the subject of a more focused and extensive future study. For $j = 3$ and 4, slightly asymmetric amphiphiles, large spherical objects are less likely to be found. Alternatively, curvature will promote elongated non-spherical morphologies. For $j = 5$, 6 mostly cylindrical morphologies are formed. The packing of these cylinders inside larger objects seems not to be crucial; we conclude that the effect of packing on the free energy is not large. In agreement with experiments, fusion of two large droplets was not found within simulation reach when the droplets are separated by solvent. Once into contact, the droplets merge by adapting their Euler characteristic (topology) and mean curvature (geometry) to one another, and form janus-like vesicles. To our knowledge, detailed experiments do not exist.

Acknowledgements

Stichting Nationale Computer Faciliteiten (NCF) is acknowledged for providing computer time on the Teras Supercomputer at SARA (Amsterdam).

References

[1] D.D. Lasic. *Nature*, **351**, 613 (1991).
[2] J. Leng, S.U. Egelhaaf, M.E. Cates. *Europhys. Lett.*, **59**, 311 (2002).
[3] J. Leng, S.U. Egelhaaf, M.E. Cates. *Biophys. J.*, **85**, 1624 (2003).
[4] R. Lipowsky. *Nature*, **349**, 475 (1991).
[5] B.R. Lentz, V. Malinin, M.E. Hague, K. Evans. *Curr. Opin. Struct. Biol.*, **10**, 607 (2000).
[6] J. Zimmerberg, L.V. Chernomordik. *Adv. Drug. Deliv. Rev.*, **38**, 197 (1999).
[7] N.S. Cameron, M.K. Corbierre, A. Eisenberg. *Can. J. Chem.*, **77**, 1311 (1999).
[8] D.E. Discher, A. Eisenberg. *Science*, **297**, 967 (2002).
[9] J.-M. Drouffe, A.C. Maggs, S. Leibler. *Science*, **254**, 1353 (1991).
[10] A.T. Bernardes. *Langmuir*, **12**, 5763 (1996).
[11] H. Noguchi, M. Takasu. *Phys. Rev. E*, **64**, 041913 (2001).
[12] S. Yamamoto, Y. Maruyama, S. Hyodo. *J. Chem. Phys.*, **116**, 5842 (2002).
[13] A.T. Benardes. *J. Phys. II France*, **6**, 169 (1996).
[14] S.J. Marrink, A.E. Mark. *J. Am. Chem. Soc.*, **125**, 15233 (2003).
[15] A.H. de Vries, A.E. Mark, S.J. Marrink. *J. Am. Chem. Soc.*, **126**, 4488 (2004).
[16] M.G. Noro, F. Meneghini, P.B. Warren. In *Mesoscale Phenomena in Fluid Systems*, F. Case, P. Alexandridis (Eds.), ACS Symposium Series, Vol. 861, pp. 242–257 (2003).
[17] S. Yamamoto, S. Hyodo. *J. Chem. Phys.*, **118**, 7937 (2003).
[18] M. Müller, K. Katsov, M. Schick. *J. Chem. Phys.*, **116**, 2342 (2002).
[19] H. Noguchi, M. Takasu. *J. Chem. Phys.*, **115**, 9547 (2001).
[20] M. Müller, K. Katsov, M. Schick. *J. Polym. Sci.: B: Polym. Phys.*, **41**, 1441 (2003).
[21] S.J. Marrink, A.E. Mark. *J. Am. Chem. Soc.*, **125**, 11144 (2003).
[22] J. Shillcock, R. Lipowsky. *Nat. Mater.*, **4**, 225 (2005).
[23] J.W. Szostak, D.P. Bartel, P.L. Luisi. *Nature*, **409**, 387 (2001).
[24] X. He, H. Liang, L. Huang, C. Pan. *J. Chem. Phys. B*, **108**, 1731 (2004).
[25] T. Uneyama, M. Doi. *Macromolecules*, **38**, 5817 (2005).
[26] G.J.A. Sevink, A.V. Zvelindovsky. *Macromolecules*, **38**, 7502 (2005).
[27] Y.Y. Wu, G.S. Cheng, K. Katsov, S.W. Sides, J.F. Wang, J. Tang, G.H. Fredrickson, M. Moskovits, G.D. Stucky. *Nat. Mater.*, **3**, 816 (2004).
[28] K. Shin, H.Q. Xiang, S.I. Moon, T. Kim, T.J. McCarthy, T.P. Russell. *Science*, **306**, 76 (2004).
[29] H.Q. Xiang, K. Shin, T. Kim, S.I. Moon, T.J. McCarthy, T.P. Russell. *Macromolecules*, **37**, 5660 (2004).
[30] H.Q. Xiang, K. Shin, T. Kim, S.I. Moon, T.J. McCarthy, T.P. Russell. *J. Polym. Sci. Part B: Polym. Phys.*, **43**, 3377 (2005).
[31] Y. Sun, M. Steinhart, D. Zschech, R. Adhikari, G.H. Michler, U. Gösele. *Macromol. Rapid Commun.*, **26**, 369 (2005).
[32] G.J.A. Sevink, A.V. Zvelindovsky, J.G.E.M. Fraaije, H.P. Huinink. *J. Chem. Phys.*, **115**, 8226 (2001).
[33] X. He, M. Song, H. Liang, C. Pan. *J. Chem. Phys.*, **114**, 10510 (2001).
[34] X. He, H. Liang, M. Song, C. Pan. *Macromol. Theor. Simul.*, **11**, 379 (2002).
[35] J. Feng, E. Ruckenstein. *Macromolecules*, **39**, 4899 (2006).
[36] P. Chen, X. He, H. Liang. *J. Chem. Phys.*, **124**, 104906 (2006).
[37] W. Li, R.A. Wickham, R.A. Garbary. *Macromolecules*, **39**, 806 (2006).
[38] B. Yu, P. Sun, T. Chen, Q. Jin, D. Ding, B. Li, A-C. Shi. *Phys. Rev. Lett.*, **96**, 138306 (2006).
[39] J.Y. Cheng, C.A. Ross, H.I. Smith, E.L. Thomas. *Adv. Mat.*, **18**, 2505 (2006).
[40] V.N. Manoharan, M.T. Elsesser, D.J. Pine. *Science*, **301**, 483 (2003).
[41] J.G.E.M. Fraaije, G.J.A. Sevink. *Macromolecules*, **36**, 7891 (2003).
[42] B.A.C. van Vlimmeren, N.M. Maurits, A.V. Zvelindovsky, G.J.A. Sevink, J.G.E.M. Fraaije. *Macromolecules*, **32**, 646 (1999).
[43] L. Zhang, C. Bartels, Y. Yu, H. Shen, A. Eisenberg. *Phys. Rev. Lett.*, **79**, 5034 (1997).
[44] G.J.A. Sevink, A.V. Zvelindovsky. *J. Chem. Phys.*, **121**, 3864 (2004).
[45] J.G.E.M. Fraaije. *J. Chem. Phys.*, **99**, 9202 (1993).
[46] J.G.E.M. Fraaije, B.A.C. Van Vlimmeren, N.M. Maurits, M. Postma, O.A. Evers, C. Hoffmann, P. Altevogt, G. Goldbeck-Wood. *J. Chem. Phys.*, **106**, 4260 (1997).
[47] G.J.A. Sevink, A.V. Zvelindovsky, B.A.C. Van Vlimmeren, N.M. Maurits, J.G.E.M. Fraaije. *J. Chem. Phys.*, **110**, 2250 (1999).
[48] B.A.C. Van Vlimmeren, N.M. Maurits, A.V. Zvelindovsky, G.J.A. Sevink, J.G.E.M. Fraaije. *Macromolecules*, **32**, 646 (1999).
[49] F. Drolet, G.H. Fredrickson. *Phys. Rev. Lett.*, **83**, 4317 (1999).
[50] G.H. Fredrickson, V. Ganesan, F. Drolet. *Macromolecules*, **35**, 16 (2002).